Towards a polarization prediction for LISA via intensity interferometry

Sandra Baumgartner [ORCID],[1]★ Mauro Bernardini,[1] José R. Canivete Cuissa [ORCID],[1,2] Hugues de Laroussilhe,[1] Alison M. W. Mitchell [ORCID],[3] Benno A. Neuenschwander,[1] Prasenjit Saha [ORCID],[3] Timothée Schaeffer,[1] Deniz Soyuer [ORCID][1] and Lorenz Zwick[1]

[1] *Center for Theoretical Astrophysics and Cosmology, Institute for Computational Science, University of Zurich, Winterthurerstrasse 190, CH-8057 Zürich, Switzerland*
[2] *Istituto Ricerche Solari Locarno (IRSOL), Via Patocchi 57, CH-6605 Locarno-Monti, Switzerland*
[3] *Physik-Institut, Universität Zürich, Winterthurerstrasse 190, CH-8057 Zürich, Switzerland*

ABSTRACT

Compact Galactic Binary Systems with orbital periods of a few hours are expected to be detected in gravitational waves (GW) by Laser Interferometer Space Antenna (LISA) or a similar mission. At present, these so-called verification binaries provide predictions for GW frequency and amplitude. A full polarization prediction would provide a new method to calibrate LISA and other GW observatories, but requires resolving the orientation of the binary on the sky, which is not currently possible. We suggest a method to determine the elusive binary orientation and hence predict the GW polarization, using km-scale optical intensity interferometry. The most promising candidate is CD–30° 11223, consisting of a hot helium subdwarf with $m_B = 12$ and a much fainter white dwarf companion, in a nearly edge-on orbit with period 70.5 min. We estimate that the brighter star is tidally stretched by 6 per cent. Resolving the tidal stretching would provide the binary orientation. The resolution needed is far beyond any current instrument, but not beyond current technology. We consider scenarios where an array of telescopes with km-scale baselines and/or the Very Large Telescope (VLT) and Extremely Large Telescope (ELT) are equipped with recently developed kilopixel sub-ns single-photon counters and used for intensity interferometry. We estimate that a team-up of the VLT and ELT could measure the orientation to $\pm 1°$ at 2σ confidence in 24 h of observation.

Key words: gravitational waves – techniques: interferometric – stars: individual: CD−30° 11223.

1 INTRODUCTION

Gravitational-wave detections are so far all transient events with no advance warning. This will change when laser interferometers in space make lower frequency gravitational waves (GW) detectable, because some Galactic binaries (known as LISA verification binaries) are predicted to be detectable via GW (Stroeer & Vecchio 2006). It would be interesting to have predictions, not only for the expected strain, but for the expected polarization as well. GW polarization is now measurable (see e.g. Abbott et al. 2017) since the Virgo interferometer has a different orientation from the two Laser Interferometer Gravitational-Wave Observatory (LIGO) detectors. In the future, it will be possible to test for additional polarization modes (see e.g. Isi, Pitkin & Weinstein 2017; Philippoz, Boîtier & Jetzer 2018), which if they exist, would imply new physics.

The GW polarization of a LISA verification binary could be predicted if the orientation of the system in the sky (inclination and position angle) were somehow measured from its electromagnetic radiation. This is where intensity interferometry comes into play. First introduced by Hanbury Brown & Twiss (1956), it was used to measure sizes of stars by counting coincident photons from an object with a pair of telescopes. By varying the separation between the telescopes, they showed that it is possible to measure the spatial

correlation function of the source brightness distribution. However, with the detectors available at the time, intensity interferometry was only feasible for some of the brightest stars, with B magnitude <2.5 (Hanbury Brown, Davis & Allen 1974). With a new generation of photon detectors now available, intensity interferometry has been revived in recent years (Zampieri et al. 2016; Weiss, Rupert & Horch 2018; Matthews, Kieda & LeBohec 2018; Guerin et al. 2018; Acciari et al. 2020; Abeysekara et al. 2020). Especially interesting is the proposal to use the Cherenkov Telescope Array (CTA) for intensity interferometry (Dravins et al. 2013), which would make baselines of up to 2 km possible.

In this paper, we propose a 'multimessenger' method to predict the GW polarization that would be observed by LISA when probing a binary system, and in particular the system CD−30° 11223, which is the optically brightest and most widely spaced of the LISA verification binaries (Kupfer et al. 2018). The system consists of a white dwarf (WD) and a hot helium subdwarf (sdB). The former is the more massive of the two objects, but contributes less than 1 per cent of the light. As a result, resolving the binary as two stars through interferometry is not a prospect, but resolving the tidal stretching of the brighter star is more promising. We suggest that, with the use of intensity interferometry, one can infer the shape of the tidally stretched sdB on the sky, thus determining the orientation of the system with respect to the Earth.

The paper is structured as follows: In Section 2, we present our method for predicting the polarization via intensity interferometry

★ E-mail: sandra.baumgartner@uzh.ch

by exploiting the tidal effects in a binary system. In Section 3, we give the system parameters of CD−30° 11223 and calculate the tidal deformation of the sdB. We present our results for various combinations of telescope arrays used for intensity interferometry in Section 4. We discuss our findings and present our concluding remarks in Section 5.

2 METHODS

2.1 The missing ingredient

The LISA mission will consist of three satellites in orbit around the Sun. Photons exchanged between the satellites carry information about their relative distances. If a GW passes through the Solar system, the photons' paths will be stretched and shrunk accordingly. This effect enables LISA to detect the passing GW. Considerable effort has been put into creating larger and more precise catalogues of expected GW signals (see e.g. Buonanno et al. 2007; Ajith et al. 2008; Huerta et al. 2017; Blanchet 2019, for different approaches). Such signals (see e.g. Filloux et al. 2012; Babak et al. 2017) originate from various types of sources (stellar mass binaries, supermassive binaries, and extreme mass ratio inspirals) located in very different astrophysical settings. Large catalogues are necessary because LISA data analysis primarily works by means of parameter fitting. Roughly described, it will detect a GW signal and then try to match it to a GW template from a catalogue (see e.g. Berti et al. 2007, for information on matched filtering). One can then trace back the properties of the source by noting what templates best fit the signal. Even though there is much talk about the capacity of LISA to test the strongest of gravitational regimes (see e.g. Berti & Cardoso 2006), it is clear that results obtained by parameter fitting must be subject to careful analysis as the process is liable to various kinds of degeneracy. Indeed, very different GW sources might produce signals that happen to be indistinguishable by parameter estimation if they are located and oriented in an inconvenient manner. Further degeneracies arise by including alternative theories of gravity, where the signal from a source in one theory might be confused with a signal from another source in a different theory. Furthermore, it is possible that some unexpected systematic error in the experimental setup would lead to systematic errors in parameter estimation, with little possibility of correction.

To get around the process of parameter fitting, it is necessary to produce a *unique* prediction for a GW signal. In other words, one must identify a promising source of GW, resolve its physical parameters with independent measurements, assume a theory of gravity and predict both the strain and the polarization amplitudes LISA would measure from it. Only such a prediction would, in principle, allow for an independent test of General Relativity. More realistically, due to uncertainties in the measurements and unknown systematics, it could be used as a calibration/validation for LISA and similar GW detectors.

As noted before, there are no sources of GW that have been completely resolved by optical methods. Even in the case of the most widely spaced LISA verification binary CD−30° 11223, the angular size is far below even the milliarcsecond scale. In particular, even though it is known that its orbital plane is almost edge on, the alignment of the plane is completely undetermined. Crucially, this remaining orientation angle controls the relative amplitude of the predicted GW polarizations. The objective of this paper is therefore set: we wish to present a method to resolve the orientation of luminous GW sources in the sky by means of intensity interferometry, thus determining the remaining physical parameter of CD−30° 11223 that is needed for a complete GW prediction.
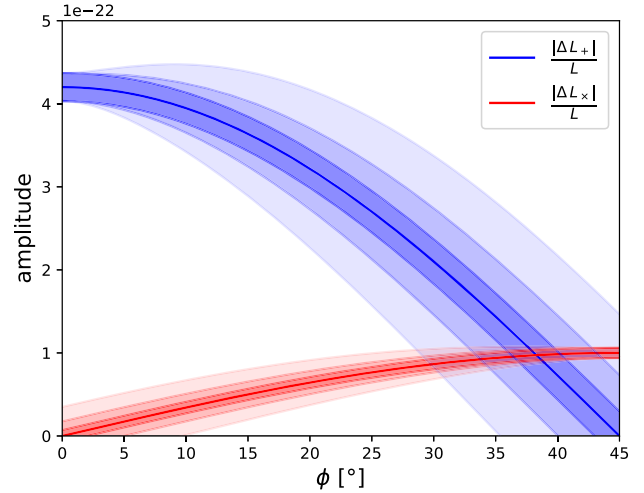

Figure 1. The full range of possible polarization amplitudes $\frac{\Delta L_+}{L}$ and $\frac{\Delta L_\times}{L}$ for the binary system CD−30° 11223 as a function of the unresolved orientation angle ϕ. The uncertainties σ_+ and $\sigma_\times$ on the prediction are represented by the shaded areas. For this plot, we have chosen three representative uncertainties in the angle ϕ of $\Delta_\phi = \{2°, 5°, 10°\}$. The lightest shades of blue and red, respectively, correspond to an uncertainty of $10°$. The figure only shows a range between $0°$ and $45°$ as the amplitudes and their errors repeat periodically in 2ϕ.

2.1.1 Coordinate system

This subsection is dedicated to the construction of a convenient coordinate system incorporating both a binary and a GW detector. For the sake of simplicity, we model the GW detector as consisting of only one arm (generalizing to more arms simply means keeping track of more angles). We align the *z*-axis of the coordinate system with the 'line of sight direction' from the binary's centre of mass to the mid-point of our idealized detector arm. This choice fixes the *x*–*y* or 'transverse' plane in which GWs will produce a measurable strain. The angular momentum vector of the binary system will in general be inclined with respect to the *z*-axis. We define the angle $\mathcal{I}$ as this inclination. We then align the *y*-axis with the projection of the orbit's angular momentum in the transverse plane. This choice of coordinates also fixes the orientation of the detector arm. It will be inclined with respect to the *z*-axis with an angle ψ and rotated from the *y*-axis with an angle ϕ. For a real space-borne detector, these last two angles will vary as the spacecraft orbits the sun.

In Fig. 1, we show how the predicted polarization amplitudes of CD−30° 11223 change for different values of the angle ϕ and different representative uncertainties Δ_ϕ (see Appendix A for a derivation), where the chosen coordinate system is illustrated in Fig. 2. In these coordinates, it is the angle ϕ that determines the polarization amplitudes and is the last missing ingredient for a polarization prediction of the binary CD−30° 11223.

2.2 Tidal stretching

In order to determine the angle ϕ, we need to devise a strategy to characterize the orbital plane of the binary system. One possible solution is given by modelling the tidal forces acting upon the stars. The total effect of gravitational interactions paired with large orbital velocities can induce stretches in the orbiting bodies due to extreme tidal forces. These deformations, if observed, can give
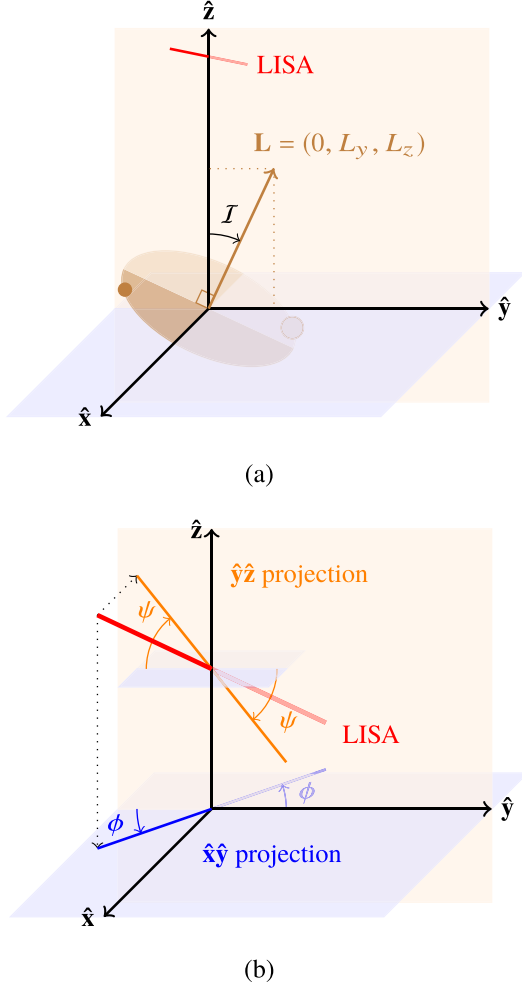
Figure 2. Illustration of the coordinate system for which the centre of mass of the binary system serves as the origin. The z-axis points towards LISA, thereby determining the propagation direction of the GW. The y-axis is chosen such that the angular momentum $\boldsymbol{L}$ of the binary system lies in the y–z plane. The angle between $\boldsymbol{L}$ and the z-axis is the inclination $\mathcal{I}$. Part (b) shows the definition of the two angles ψ and ϕ related to LISA (red line). The blue and orange lines are the projections of LISA on to the x–y and the y–z planes, respectively.

precise information about the orbital plane, and consequently the angle ϕ.

In the following paragraphs, we present two distinct approaches to estimate the induced deformation.

2.2.1 Roche potential

The Roche potential offers an analytic description for the gravitational potential of two tidally locked, corotating bodies on circular orbits with common orbital period ω. If the masses M_1, M_2 and the separation a of the binary stars are known, the Roche potential takes the form:

$$\Phi(\boldsymbol{r}) = -\frac{GM_1}{|\boldsymbol{r}-\boldsymbol{r}_1|} - \frac{GM_2}{|\boldsymbol{r}-\boldsymbol{r}_2|} - \frac{1}{2}\omega\,|\boldsymbol{r}|^2 \quad (1)$$

where $\omega^2 = G(M_1 + M_2)/a^3$ is the orbital frequency and $\boldsymbol{r}_1$ and $\boldsymbol{r}_2$ denote the positions of the stars. For each one of the binary objects, the tidal deformation redistributes the mass such that on the surface the potential is constant. This specific enclosing equipotential

line exactly describes the deformed shape of the star. We solve the problem of finding this specific value numerically by scanning the range of equipotential lines. The desired potential has to fulfill the condition that the enclosed mass corresponds to that of the undeformed case. If we neglect other sources of deformation (e.g. fast rotation and oscillations), the general shape of the star will follow a teardrop Roche lobe. We aim to measure the ratio κ between the major and minor axis of the object, which we define as $r_{\max}$ and $r_{\min}$, respectively. This can be easily computed once the deformation of the object is known. In most practical cases, we can approximate the shape to a spheroid.

2.2.2 Variations in radiant intensity in the direction of the observer

Another approach to determine the deformation caused by tidal stretching is to study variations in the radiant intensity in the direction of the Earth. As the visible area of the star changes during one orbital period due to its deformed shape, the received light on Earth changes accordingly. The ratio between the major and minor axes can then be computed by comparing the minimal and maximal value of this flux.

Let us assume a spheroid shape for the deformed star and model it as a perfect blackbody. If the two orbiting bodies are aligned with the line of sight of the observer, the area of the star visible from the Earth is $A_{\min} = \pi r_{\min}^2$ and therefore the radiant intensity in the direction of the Earth is proportional to $I_{e,\Omega}^{\min} \propto \sigma A_{\min} T_{\mathrm{eff}}^4$, where σ and T_{eff} denote the Stefan–Boltzmann constant and the effective stellar temperature. Conversely, if the two stars are placed in a plane perpendicular to the line of sight, then the observed shape corresponds approximately to an ellipse of area $A_{\max} = \pi r_{\min} r_{\max}$, and the radiant intensity in the direction of the Earth is proportional to $I_{e,\Omega}^{\max} \propto \sigma A_{\max} T_{\mathrm{eff}}^4$. Given that the distance to the sdB is practically constant, we link the observed flux variations directly to the ratio between the axes $r_{\min}$ and $r_{\max}$:

$$\frac{I_{e,\Omega}^{\min}}{I_{e,\Omega}^{\max}} = \frac{A_{\min}}{A_{\max}} = \frac{\pi r_{\min}^2}{\pi r_{\min} r_{\max}} = \frac{r_{\min}}{r_{\max}} = \kappa\,. \quad (2)$$

We discuss the case of the CD$-30°$ 11223 binary system in Section 3 below.

These two methods provide independent ways of estimating the aspect ratio between $r_{\min}$ and $r_{\max}$, as the first relies on theoretical background and the second is based on observational data. This allows one to cross-check the results. However, uncertainties arise in both procedures as simplifications are made. The fact that this ratio will often be close to unity gives rise to significant observational challenges, which we hope to surmount with the aid of intensity interferometry. A good estimate of this aspect ratio is essential for measuring the orientation of the binary in space, which in turn is needed for a polarization prediction of the GW.

2.3 Intensity interferometry

To appreciate the challenge of determining the orientation of the orbital plane, consider first a fictitious binary consisting of two touching Sun-like stars in a circular orbit ($M_1 = M_2 = M_\odot$, $a = 2\,R_\odot$) observed from a distance of $D = 50\,\mathrm{pc}$. The angular size and the GW frequency and strain of a binary are:

$$\theta \sim \frac{a}{D} \qquad f \propto \left(\frac{a^3}{M_1 + M_2}\right)^{1/2} \qquad h \propto \frac{M_1 M_2}{aD} \quad (3)$$

respectively. For this fictitious system, the values come to

$$\theta \sim 10^{-9}\,\mathrm{rad} \qquad f \propto 10^{-4}\,\mathrm{Hz} \qquad h \propto 10^{-22}. \quad (4)$$

Current optical interferometry of binary stars (e.g. Lester et al. 2019) achieves a resolution of 0.2 mas $\approx 10^{-9}$ rad, so this imaginary system would be borderline resolvable. In GWs, however, it would be too weak/slow to detect with any planned instrument. For a mission lifetime T_{obs} of a few years, the characteristic strain $h\sqrt{f T_{obs}} \sim 10^{-20}$. LISA and TianQin are expected to reach this level of sensitivity, but only at higher frequencies — see fig. 1 in Robson, Cornish & Liu (2019) for LISA and fig. 2 in Hu et al. (2018) for TianQin. In comparison with this imaginary system, real LISA verification binaries are an order of magnitude closer in orbital separation and an order of magnitude further away from us. This makes them much too small on the sky for current optical interferometry to resolve. A possible way to achieve much higher resolution is by means of *intensity* interferometry. This technique was developed in the 1960s (for the historical development, see Hanbury Brown 1974). The detector technology of the time limited its applicability to about 30 blue stars, but the sources that could be observed were resolved to ~ 0.5 mas.

The main idea behind intensity interferometry involves *temporally* correlating the light signals received by a pair of telescopes, separated by a baseline. The measured intensities in both telescopes $\langle I_1 \rangle$ and $\langle I_2 \rangle$ (which are averaged over a time-scale, characteristic of the setup; the resolution time) will have a cross-correlation profile $\langle I_1 \cdot I_2 \rangle (r_1 - r_2)$ dependent on the projected baseline $\boldsymbol{B} = \boldsymbol{r}_1 - \boldsymbol{r}_2$ between the telescopes. As is well known in quantum optics (see e.g. Mandel & Wolf 1995), assuming a chaotic light source (which is valid for thermal astrophysical sources, see Dravins et al. 2013; Foellmi 2009), one can relate the cross-correlation of the intensities $\langle I_1 \cdot I_2 \rangle$ to the absolute square of the spatial correlation function $|\gamma_{12}|^2$ between the two telescopes:

$$\langle I_1 \cdot I_2 \rangle = \langle I_1 \rangle \langle I_2 \rangle (1 + |\gamma_{12}|^2) \tag{5}$$

Since the source is assumed to be chaotic, the intensity fluctuations will average out over time-scales which are much longer than the coherence time of light. Thus, per definition: $\langle \Delta I \rangle = \langle I - \langle I \rangle \rangle = 0$. The cross-correlation of the intensity fluctuations ΔI_1 and ΔI_2 will be:

$$\langle \Delta I_1 \cdot \Delta I_2 \rangle = \langle I_1 \rangle \langle I_2 \rangle |\gamma_{12}|^2 \tag{6}$$

If one has a continuous source, then $|\gamma_{12}|^2$ corresponds to the correlation of photons coming from different small elements of the source's image on the sky. It will be identical to the the Fourier magnitude of the source distribution Σ:

$$|\gamma_{12}|^2 = \left(\mathcal{F}[\Sigma] \right)^2. \tag{7}$$

We can write down the spatial separation of the two telescopes with respect to the line of sight to the source for an optical wavelength λ, as defined in Dravins et al. (2013): $\boldsymbol{B} = \lambda \cdot (u, v, w)$. The w component accounts for the time delay due to the obliqueness of the telescope plane. Thus, the $(u, v, w = 0)$ plane represents the scenario where the line of sight lies perpendicular to the plane on which the telescopes lie. Fig. 3 demonstrates how the spatial correlation function of an elliptical source distribution of a few microarcseconds is represented in the $(u, v, 0)$ plane. For a source of angular diameter δ, the characteristic scale up to which $|\gamma_{12}|^2$ is significantly non-zero in the (u, v) plane is λ/δ. In principle, one could choose to use a wavelength that best conforms to a given range of baselines and source angular size. In practice, astrophysical sources shine the brightest in a particular colour and detectors are often optimized in a single band for intensity interferometry. These effects restrict the free choice of the wavelength. Considering a 350 -nm optical wavelength, a 5 -km baseline will reach a resolution of about 10 μas.

The relationship between the (u, v, w) vector and the baseline projections is given by the product rotation:

$$\begin{pmatrix} u \\ v \\ w \end{pmatrix} = \frac{1}{\lambda} R_x(\delta) R_y(h) R_x(-l) \begin{pmatrix} B_E \\ B_N \\ B_{up} \end{pmatrix} \tag{8}$$

where

$$R_x(\delta) = \begin{pmatrix} 1 & 0 & 0 \\ 0 & \cos\delta & -\sin\delta \\ 0 & \sin\delta & \cos\delta \end{pmatrix} \tag{9}$$

and similarly for $R_x(-l)$ while

$$R_y(h) = \begin{pmatrix} \cos h & 0 & \sin h \\ 0 & 1 & 0 \\ -\sin h & 0 & \cos h \end{pmatrix} \tag{10}$$

where l is the latitude of the setup, δ is the declination, and h is the hour angle of the source. Expanding out the product, equation (8) is equivalent to equation (7) from Dravins et al. (2013).

2.3.1 A hypothetical telescope array

Since intensity interferometry has already been proposed for the CTA, we will use its telescope configuration as an example to demonstrate our method. We consider a hypothetical array of Cherenkov telescopes, the Array for CHerenkov Shower Observations (ACHSO), located at the proposed Chilean site for CTA, with the same telescope layout and subsequent number of baselines available. This comprises four large-sized telescopes (23 m), 25 medium-sized telescopes (12 m) and 70 small-sized telescopes (4 m) (see Acharya et al. 2013). The array layout can be seen in top left of Fig. 4. The total number of baselines in this case turns out to be: $n(n-1)/2 = 4851$, where $n = 99$ is the total number of telescopes in the array. However, for the purposes of this measurement we assume a considerably improved optical performance (point spread function, PSF and *f*-number) over that typical for Imaging Atmospheric Cherenkov Telescopes (IACTs). This renders ACHSO a much more suitable array for optical intensity interferometry. In the results sections we will also explore various combinations of the ACHSO, Very Large Telescope (VLT) and Extremely Large Telescope (ELT). Within our assumptions, applying our method to different arrays simply requires adjusting the baselines and the collecting areas of the telescopes.

Arrays of Cherenkov telescopes are gamma-ray facilities designed to detect the Cherenkov emission produced by Extensive Air Showers generated by gamma rays entering the Earth's atmosphere. IACTs, are designed to detect these faint Cherenkov flashes – as the spectrum of Cherenkov light lies in the optical wavelength band (peaking towards the blue end), IACTs are sensitive optical instruments, with large mirror reflectors. The coherent wavefront of Cherenkov radiation from Extensive Air Showers typically reaches the ground within a few ns; accordingly the standard cameras employ fast imaging techniques to capture images of the air shower. For intensity interferometry, however, continuous signal integration is necessary, requiring a different data acquisition process to the short readout windows used in Cherenkov observations. Currently, options to incorporate intensity interferometric capabilities are being explored, either as an alternative operation mode of the cameras or as separate equipment mounted on the lid of the cameras when they are closed (Dravins et al. 2013). Existing IACT arrays have recently made astrophysical measurements, demonstrating the feasibility of conducting intensity interferometry with a removable plate that can be easily
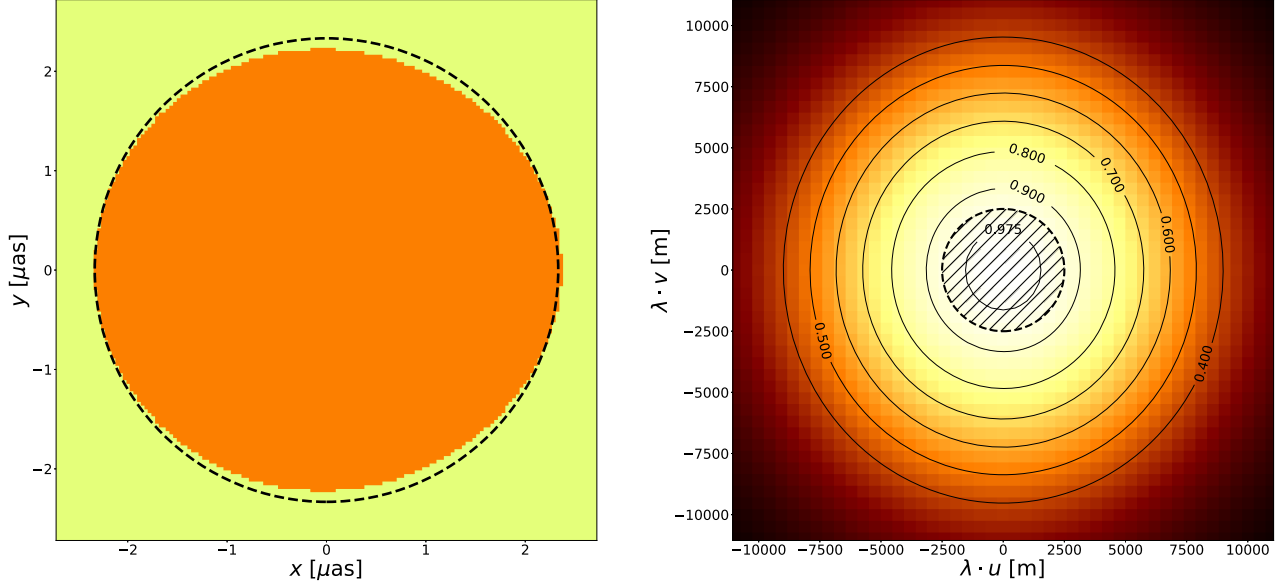
Figure 3. Left: simulated noise-free image of a uniformly emitting extended source at $\lambda = 350$ nm in orange. Note that the source is teardrop shaped, same as that calculated for CD–30° 11223 in the next sections. The dashed black curve shows the shape the same object would have in the absence of tidal disruptions. Right: the Fourier magnitude $|\gamma_{12}|^2$ of the source in the (u, v) plane. Contours show how the magnitude decreases with distance from the centre. Not shown in these scales is the full teardrop-shaped Airy pattern, which extends beyond 14 km, having visible local minima and maxima. The dashed area indicates the coverage of the baselines by CTA-S.

added to the Cherenkov camera focal plane (Matthews & LeBohec 2019; Kieda, LeBohec & Cardon 2019). Intensity interferometry with IACTs works well given their comparatively good mirror reflectivity, of typically > 85 per cent in the optical wavelength range Gaug et al. (2019). However, the sensitivity towards ~12 mag objects is only achievable with the improved optical properties provided by ACHSO. With regards to the PSF, we estimate that in order to reduce the background noise contribution to a level significantly below that of a mag ~12 source, the PSF of ACHSO needs to be improved by a factor ~100 over current IACT instrument performance. This is because, when observing under moonlight, the background brightness amounts to ~17 mag arcsec^{-2}. Alternatively, the source could be observed under dark sky conditions, when the background contribution per square arcsecond is ~5 mag less. This requirement can, however, be alleviated somewhat by the use of a narrow-band filter, to reduce the broad-band night sky background contribution to the signal in the wavelength range of interest.

As the Cherenkov light from Extensive Air Showers is particularly faint, observations are sensitive to background light from stars and can be severely affected by moonlight, to the extent that observations typically do not take place when the moon is illuminated at high percentages or high above the horizon. Although disadvantageous for gamma-ray observations; it may be feasible to employ this time for intensity interferometry, unless otherwise needed for calibration purposes (Dravins et al. 2013). Nevertheless, the overall technological adjustments are comparatively minor and non-invasive to the primary purpose of IACT arrays as gamma-ray facilities. Dravins et al. (2013) outline and discuss the adjustments necessary to successfully operate as an optical interferometric instrument.

2.3.2 Signal-to-noise estimation

The signal-to-noise (S/N) ratio in interferometry has an interesting dependence on the source and instruments. Let n be the spectral photon flux of the source (photons m^{-2} s^{-1} Hz^{-1}) and let $|\gamma_{12}(\mathbf{r})|^2$ be

the normalized correlation. Let A be the area of each light bucket (the geometric mean if not equal), $\Delta \nu$ the observing optical bandwidth, α is the quantum efficiency of the photon detectors, Δf the electronic bandwidth (i.e. reciprocal of the resolution time), and $N_t = \Delta f \times T$ (where T is the integration time) is the number of time slices used to measure the signal. Then:

$$\left(\frac{S}{N}\right)_{RMS} = A\,\alpha\,n\,|\gamma_{12}(\mathbf{r})|^2 \sqrt{\frac{N_t}{2}}. \tag{11}$$

for a single spectral channel (see e.g. Le Bohec & Holder 2006). A more detailed expression is given by Hanbury Brown & Twiss (1957) in their equation (3.62). We can express the signal amplitude as:

$$S = (A\,\alpha\,n)^2\,|\gamma_{12}(\mathbf{r})|^2\,\frac{\Delta \nu}{\Delta f}\,N_t \tag{12}$$

whose interpretation is the expected excess of correlated photons in time T. The noise amplitude is:

$$N = A\,\alpha\,n\,\frac{\Delta \nu}{\Delta f}\,\sqrt{2N_t}, \tag{13}$$

and comes from the shot noise in the number of correlated photons. Both S and N here are dimensionless, and differ from the corresponding expressions in Hanbury Brown & Twiss (1957) by a dimensional factor.

The quantum efficiency of the photomultiplier tubes at the CTA are around 40 per cent at 350 nm wavelength, whilst the SiPMs used by the smallest telescopes can have an efficiency of up to 50 per cent at 470 nm (Sakurai, Depaoli & López-Coto 2019; Heller et al. 2017). Recently, Wollman et al. (2019) report a 1024-channel detector using superconducting nanowires with a time resolution better than 0.5 ns ($\Delta f \sim 2 \times 10^9$ Hz). The detection efficiency of these is only up to 23 per cent so far, but is expected to improve considerably as the technology is developed further. As part of ACHSO, we consider that such nanowire detectors can in principle be installed on all telescopes. Moreover, new technologies may enable more channels with better time resolution and more efficient photon detectors might
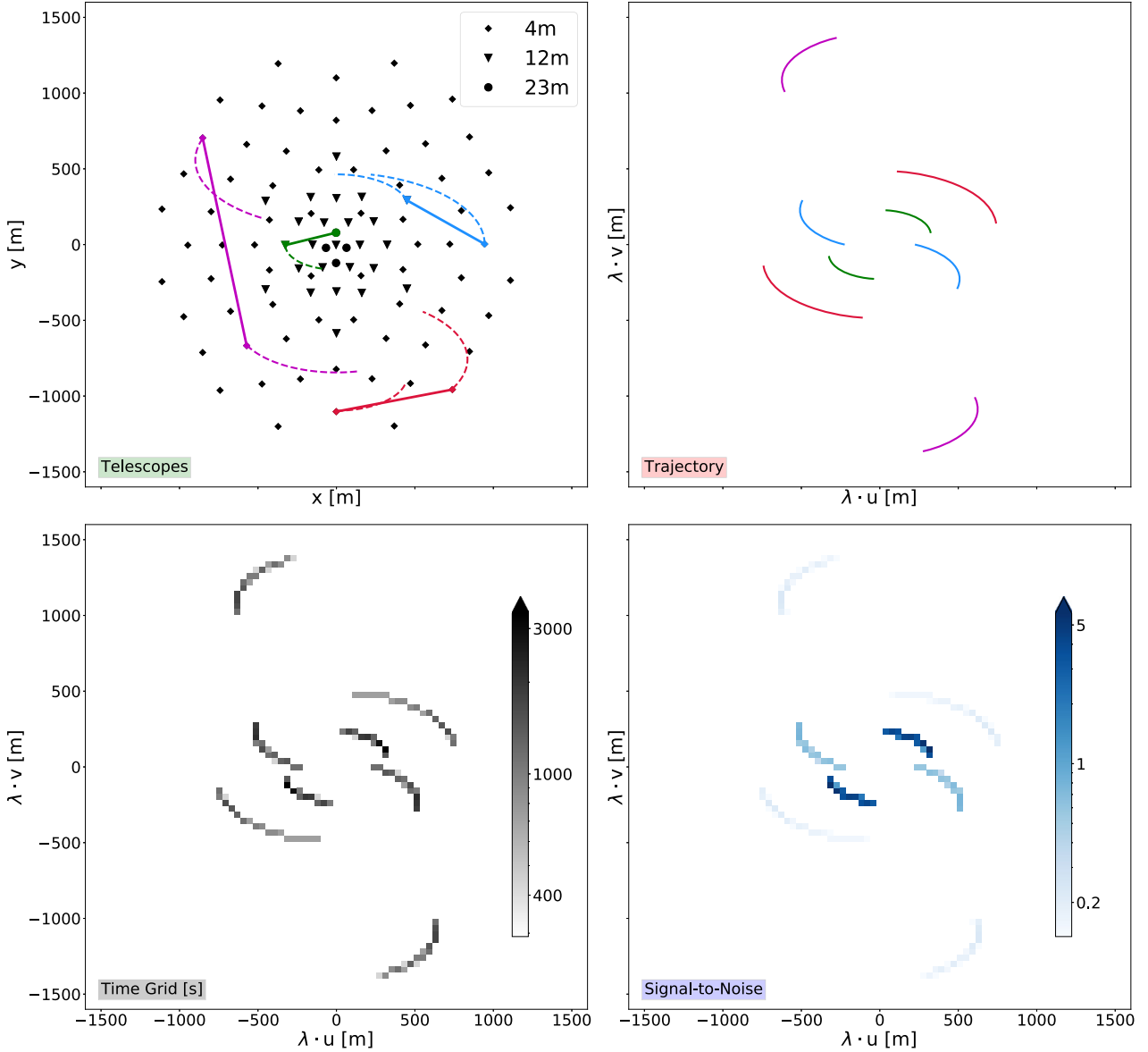
Figure 4. Top left: layout of the hypothetical telescope array ACHSO in the Southern hemisphere. Four different baselines are highlighted for demonstration purposes with solid lines with the integration time set to ∼5 h. Depending on where the source is located in the sky, the Earth's rotation induces a sweeping motion on the plane. The resulting trajectories for a source with a declination of 30° are shown with dashed lines. Top right: the trajectories of the selected baselines in the (u, v) plane. Note that the lines here are not the same ones as the dashed lines in the top left panel, but rather they represent the sweeping of the 'baseline' due to Earth's rotation. Bottom left: the time grid of the selected baseline trajectories projected on to pixels. Bottom right: the S/N ratio on the individual pixels with the same integration time and using 1024 channels per detector (S/N $\propto \sqrt{N_{\text{channel}}}$).

be developed prior to the launch of LISA. We further assume that the main mirrors are isochronous to better than the detector time resolution.

2.3.3 Parameter fitting

We will now demonstrate that it would be possible to deduce the orientation of the source in the sky from the variations of $|\gamma_{12}(\boldsymbol{r})|^2$ over the (u, v) plane using intensity interferometry. Hanbury Brown (1974) already applied the basic idea applied to the rotational flattening of Altair (see his section 11.7). In this work, we have developed a fitting technique that combines the data collected by all the available ACHSO pairs of telescopes. Due to the rotation of the

Earth, each baseline moves in the (u, v) plane. Knowing the position of the binary in the sky and the coordinates of ACHSO, we can compute the trajectories of the baselines using equation (8). They cover the (u, v) plane in an inhomogeneous way as shown in the top left corner of Fig. 4. We discretize the problem and divide the (u, v) plane into small pixels with area ≈ 40 m × 40 m. Considering one night of observation time, we account for the fraction of time each pair of detectors spends collecting data in each pixel. We then obtain an effective integration time t_{ij} at each grid point in the (u, v) plane. Thus

$$\sum_{i,j} t_{ij} = N_B \cdot T, \tag{14}$$

where N_B is the number of pairs (baselines) and T the observation time. This procedure holds only if the area of the pixels we choose is at least as big as the smallest telescope of the detector. The S/N adds in quadrature, therefore we end up with an effective S/N for each pixel that takes the simple form of equation (11) using t_{ij} as a local integration time and the mean area of the telescopes that eventually crossed the pixel as the effective collecting area. We then perform a likelihood analysis of a mock signal with known orientation ϕ_0 to estimate our capacity to reproduce the true value.

We first generate a signal for a given layout of telescopes, using equation (12). In order to model a realistic measurement, this noiseless signal must be completed with noise characterized by equation (13). Given the source flux of CD−30° 11223, and the layout of the ACHSO; a baseline consisting of telescopes with 4-m diameter, located in the (u, v) plane such that $\gamma = 0.5$, will receive approximately 16 coincidence photons per hour.

The number of coincident photons pairs that arrive on two detectors is a Poisson process. However, since the number of events detected during a significant integration time with each baseline will be large enough, it is acceptable to model the noise with a Gaussian distribution. This $S + N$ constitutes the mock data s_{ij}^{ϕ}, from which we aim to fit the corresponding angle ϕ. We then generate a set of noiseless signals that span the full range of possible orientations. For a test signal with orientation θ, assuming a flat prior, the total posterior distribution is the product of the likelihood of each pixel:

$$P(\theta|\phi) = \prod_{i,j} \mathcal{L}_{ij}(\phi|\theta) = \prod_{i,j} \frac{1}{2\pi \sigma_{ij}^2} \exp\left[-\frac{\left(s_{ij}^{\theta} - s_{ij}^{\phi}\right)^2}{2\sigma_{ij}^2}\right] \quad (15)$$

where $\sigma_{ij} \propto t_{ij}^{-1/2}$ is the standard deviation of s_{ij}^{ϕ}, obtained from equation (13) using the effective integration time. The most likely value of θ will tend to the true value as a function of observation time.

3 BINARY SYSTEM CD−30° 11223

As a proof of concept, we want to apply the methods presented in Section 2 specifically to the brightest LISA confirmation binary system, CD−30° 11223.

This system hosts a WD and a hot helium sdB orbiting each other in a binary fashion. As summarized in Table 1, the configuration of the system is such that the two bodies are close with a comparatively short orbital period, making it suitable for LISA's verification tests (Kupfer et al. 2018). Moreover, the total effect of gravitational interactions paired with large orbital velocities generates extreme tidal forces which stretch the sdB. Therefore, the configuration of CD−30° 11223 makes it a promising candidate to infer the angle ϕ of the system from intensity interferometry within a reasonable amount of observational time.

In the following, we apply the approaches described in Section 2.2 to estimate the induced deformation of the sdB. The Roche potential offers an analytic description for the gravitational potential of two tidally locked, corotating bodies on circular orbits with common orbital period ω. Since the orbital period of CD−30° 11223 is significantly smaller than 10 d, the assumption of a circular orbit and tidal locking for the sdB is justified according to Zahn (1989). We thus implement the pipeline using the classical Roche potential presented in Section 2.2 as both conditions are fulfilled for the CD−30° 11223 system. However, we note that one could adopt a more generalized Roche potential as presented by Avni & Schiller (1982) to relax

Table 1. Parameters of the binary system CD−30° 11223. The two solutions are obtained with (Intermediate-dispersion Spectrograph and Imaging System) ISIS, and Goodman, a spectrograph at the Southern Astrophysical Research (SOAR) telescope, and allow to investigate systematic errors. However, only solution 2 is used in this study (Geier et al. 2013) and [†](Kupfer et al. 2018).

sdB temperature	$T_{\rm eff}$	$29.2(4) \times 10^3$	K
Orbital period	P	1.175497738(40)	h
Parallax [†]	d	2.963(80)	mas
Solution 1			
sdB mass	$m_{\rm sdB}$	0.47(3)	$M_\odot$
sdB radius	$R_{\rm sdB}$	0.169(5)	$R_\odot$
WD mass	$m_{\rm WD}$	0.74(2)	$M_\odot$
WD radius	$R_{\rm WD}$	0.0100(4)	$R_\odot$
Separation	a	0.599(9)	$R_\odot$
Orbital inclination	$\mathcal{I}$	83.8(6)	°
Solution 2			
sdB mass	$m_{\rm sdB}$	0.54(2)	$M_\odot$
sdB radius	$R_{\rm sdB}$	0.179(3)	$R_\odot$
WD mass	$m_{\rm WD}$	0.79(1)	$M_\odot$
WD radius	$R_{\rm WD}$	0.0106(2)	$R_\odot$
Separation	a	0.619(5)	$R_\odot$
Orbital inclination	$\mathcal{I}$	82.9(4)	°

some of the restrictive orbital assumptions in order to model binary systems with more extreme cases of misalignments.

On the top left of Fig. 5 we show the equipotential lines computed numerically given the parameters of the second solution of the binary listed in Table 1, while on the top right we zoom on the sdB and show the actual deformation caused by tidal forces. On the bottom, we show the radial deformation, given by the ratio between the radius at azimuthal angle ξ and the mean radius $r_{\rm sdB}$. We see that the deformation function does not precisely follow a cosine, since the true shape of the sdB will be a Roche lobe. However, to first order, the spheroidal approximation holds. We can therefore compute the ratio κ between the minor and major semi-axes, $\kappa = r_{\rm min}/r_{\rm max}$. From the two solutions of the binary, we obtain the following numerical results:

$$\kappa_1 = 0.940(1) \qquad \kappa_2 = 0.940(3) \quad (16)$$

As a confirmation, we apply the brightness variation method described in Section 2.2 to the V-band light-curve data presented in Geier et al. (2013, fig. 5), where the major fluctuations are precisely due to tidal effects. With the data available we estimate:

$$\kappa = \frac{I_{e,\Omega}^{\rm min}}{I_{e,\Omega}^{\rm max}} = 0.923(3) \quad (17)$$

which is in the same range as the result obtained with the more sophisticated numerical approach presented above. We would like to make the reader cautious about the fact that the errors presented in equations (16) and (17) are only due to measurement uncertainties. Therefore, the difference between the values of the two estimates comes from the different assumptions made for the two methods, which we discuss in what follows.

The calculated values of κ are subject to different error sources. The Roche potential approach suffers mainly from uncertainties related to the observed properties of the binary system. Although smaller contributions are expected to arise from potential perturbations caused by the star deformations. In fact we compute the potential assuming point mass objects. In this particular case these effects are negligible, since the shape of the WD is essentially spherical and not perturbed by the sdB. In general, this method
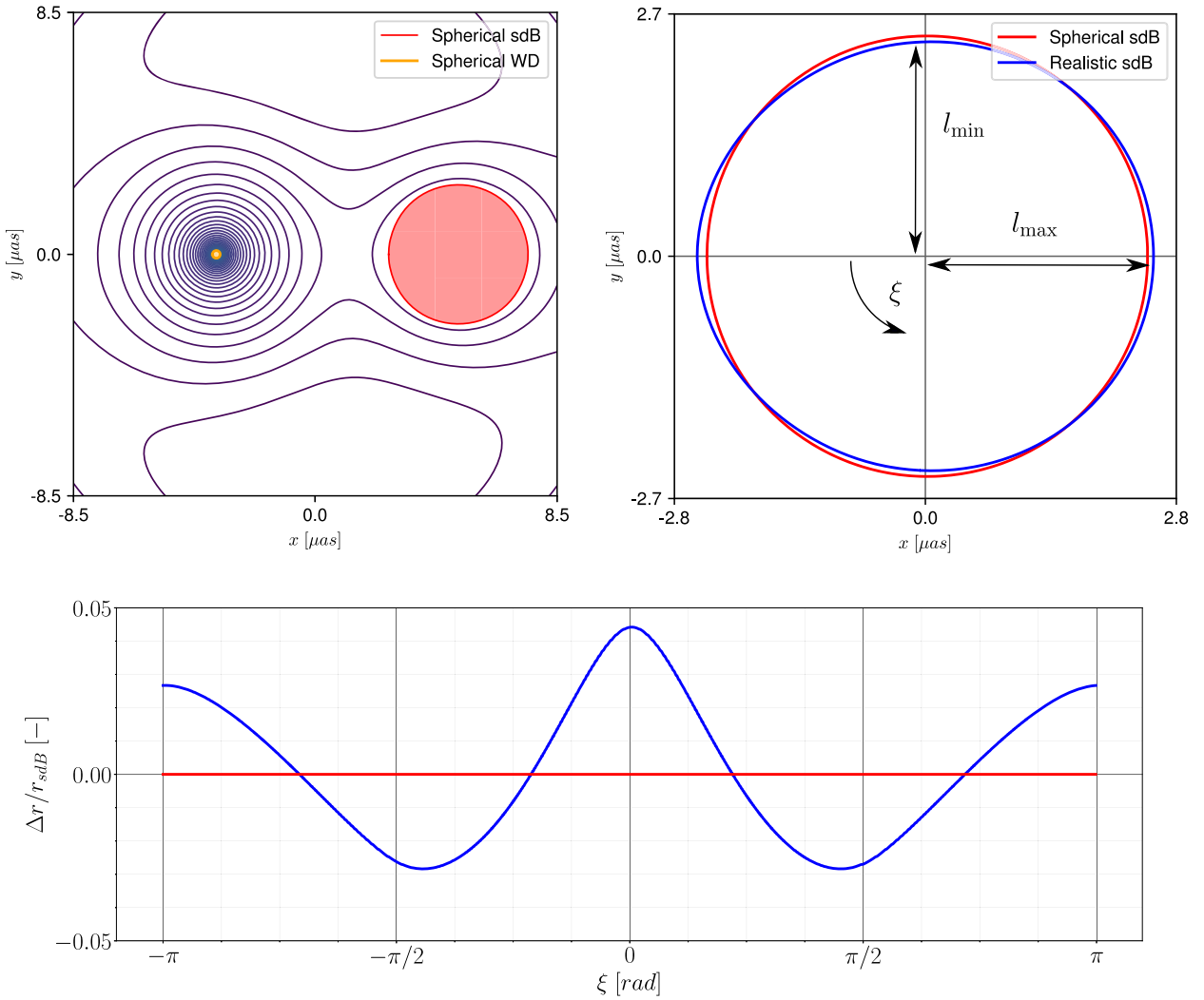
Figure 5. Top left: representation of the Roche equipotential lines for the binary system CD–30° 11223. The spherical approximated shapes of the WD (in yellow) and the sdB (in red) are shown. Top right: representation of the realistic shape of the sdB deformed by the tidal forces. The major and minor semi-axes, r_{min} and r_{max}, are presented for the spheroid approximation. $\xi = 0$ indicates the direction towards the WD. Bottom: relative deformation from the spherical approximation computed as $\Delta r/r_{sdB}$ as a function of the angle ξ.

is reliable for sufficiently precise measurements of its principle properties as the mass, radius, and separation of the stars.

Concerning the variation in radiant intensity in the direction of the Earth, the uncertainty in the estimation of κ is of the same order of magnitude as the Roche potential method, given the available data. However, this method is based on a simplistic physical model and therefore ought be considered approximate. First, it relies again on the accuracy of the measured flux. Secondly, relativistic Doppler boosting effects can vary the flux maxima and minima during the system's revolution. However, as we can seen from fig. 5 of Geier et al. (2013), such an effect is negligible with respect to the variations due to the spheroidal deformation. Thirdly, the body shape is assumed to be spheroidal and its radiative spectrum follows the one of a perfect blackbody. Furthermore the effect of limb-darkening on the flux, and therefore on the estimated area, is neglected. In conclusion, this method is rather approximate and should be used solely as an order-of-magnitude estimation.

4 RESULTS

4.1 Observation time calculations

We consider ACHSO in a scenario corresponding to the planned configuration for CTA (South), with 99 telescopes (4851 different baselines) spread over $4\,km^2$. We assume all the telescopes are able to observe in 1024 spectral channels with a time resolution of 0.5 ns (cf. Wollman et al. 2019) and that the background and all systematic effects are much less than the counting noise (equation 13). For simplicity, we also assume that all hour angles are accessible over the course of a year (in effect, taking the source to be circumpolar); this is not true for CD−30° 11223 at the site latitude, but is not expected to significantly change our estimates.

We generate a noisy $|\gamma_{12}|$ with equation (7) given the stretched geometry of the star, assuming the true binary orientation corresponds to $\phi = 0$. We then compute the posterior probability (equation 15) for inferring ϕ. Fig. 6 shows the posterior for the binary orientation for
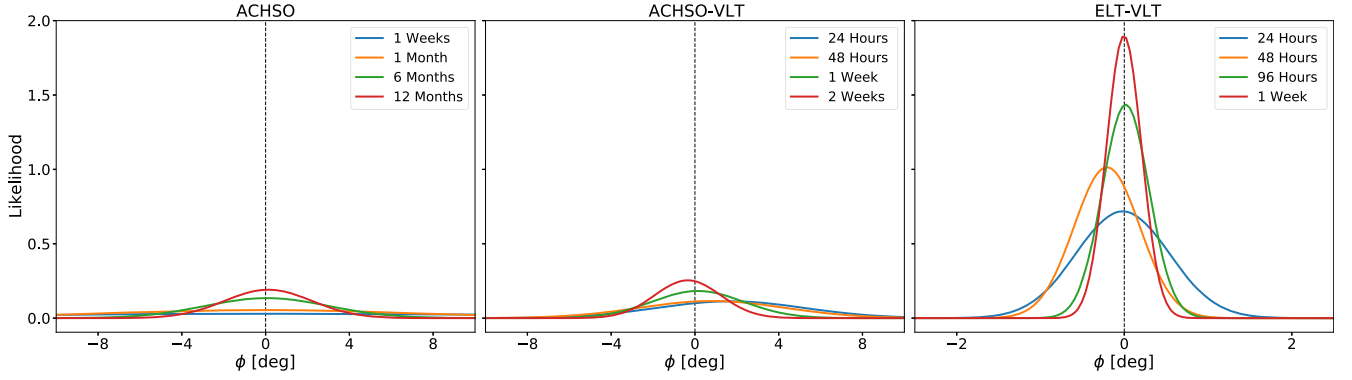
Figure 6. We plot the posterior probability distributions (PDs) of the orientation angle ϕ obtained by fitting different mock signals with the same assumed prior value of $\phi_0 = 0°$ (represented by the dashed line). The Gaussian PDs are constructed assuming various number of nights of observations for different combinations of telescope arrays: ACHSO only (left-hand panel), ACHSO-VLT (central panel), and ELT-VLT (right-hand panel).
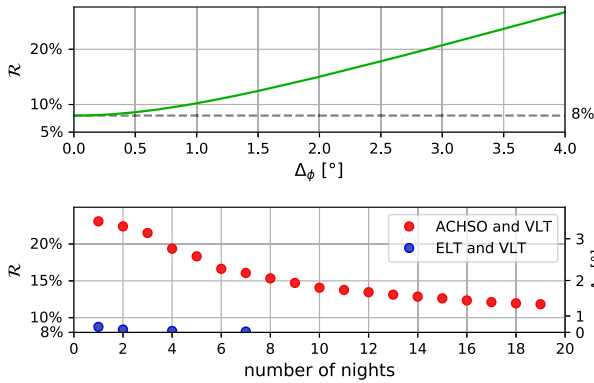

Figure 7. Here, we plot the uncertainty $\mathcal{R}$ (equation 19) of the polarization prediction both as a function of Δ_ϕ (top panel) and observation time (bottom panel), where Δ_ϕ is the 1σ uncertainty in the inferred angle. From the upper panel, one sees that the mean square uncertainty increases rather sharply for an error Δ_ϕ larger than a few degrees. The dashed 8 per cent uncertainty line is due to measurement errors listed in Table 1. The lower panel shows that the combination of ACHSO and VLT can essentially remove the error due to the measurement of the orientation angle in a dozen observation nights, while the ELT+VLT take only a fraction of an observation night to reach 1σ confidence levels.

various observation times, ranging from one week to twelve months,[1] using the ACHSO. A measurement of the binary orientation with an uncertainty of $\pm 5°$ at 1σ confidence level, would require the full ACHSO layout for about one month. Admittedly, this does not seem very promising, but could still be an interesting constraint for the polarization predictions (see Fig. 1). In Fig. 7, we show how the constraints on the angle ϕ get better with more observation time.

Although we can assume that the background light is insignificant for ACHSO, this is unfortunately unlikely to hold for the true CTA because the expected PSF would let in significant amounts of background light from the sky. The PSF has two origins. One is spherical aberration and so on from the mirror figure, which as an isolated effect, could in principle be corrected using customized secondary mirrors, as was done in the *Hubble Space Telescope* (see figs 1-3 in Jedrzejewski et al. 1994). However, the other contribution to the PSF is the roughness of the mirror surfaces, which cannot be compensated for and is a limiting factor that also prohibits the

use of secondary optics to correct for spherical aberrations. Mirrors for normal telescopes are polished to subwavelength smoothness, but because of the cost of optical-quality polishing, Cherenkov air telescopes polish only enough to keep the PSF acceptable for imaging Cherenkov showers: $\approx 10^{-3}$ rad or ≈ 3 arcmin, that is, comparable with naked-eye seeing (see e.g. Tayabaly et al. 2015; Rou et al. 2013). If the night sky within the PSF is comparable to or brighter than a given source, the photon noise scales with the PSF, and as a result the observation time-scales with the area in the PSF. For the PSF of typical IACTs, simulations by Rou et al. (2013) indicate that for sources beyond magnitude 10, the observing times needed become impractical and source confusion between stars within the field of view also starts to become an issue. The PSF quality is therefore a fundamental difference between CTA and ACHSO.

4.2 Multi-array combinations

In this section, we will explore two combinations of ACHSO, VLT, and ELT. Considering multi-array combinations allows us to cover a significantly broader region of the (u, v) plane, due to the longer base lines. Moreover, optical telescopes such as VLT and ELT have superior mirrors and a low PSF. We start with the combination of ACHSO and VLT.

The VLT is made of four 8-m telescopes, in the Atacama desert, ~ 11 km away from ACHSO. We assume the same quantum efficiency and bandwidths for both arrays and carry out the analysis proposed in Section 2.3.3 including all the baselines between the pairs of telescopes. Fig. 6 shows the likelihood estimation of the binary orientation for various observation times using ACHSO combined with the VLT. We obtain drastically better results for the estimation of ϕ. As an example, the uncertainty in the measurement falls down to $\pm 3°$ at 2σ in just one week of observation. In Fig. 7, we show how the constraints on the angle ϕ get better with more observation time.

Even more powerful is the combination of VLT and ELT. The ELT is made of a 39.3-m telescope, in the Atacama desert, ~ 21 km away from the VLT. We assume the same quantum efficiency and bandwidths for it, and carry out the analysis proposed in Section 2.3.3 for the four baselines between the ELT and VLT telescopes. Fig. 6 shows the likelihood estimation of the binary orientation for various observation times. Due to the long baselines and the large collecting areas of VLT and ELT, we obtain an extremely precise constraint on the orientation angle ϕ in a very short observation time: an uncertainty of $\pm 1°$ at 2σ is reached in roughly 24 h of observations,

[1]For a month, we assume 30×12 h of observing time.

while the same uncertainty at $5\,\sigma$ is reached in roughly five nights (60 h) of observation.

4.3 Polarization prediction for CD−30° 11223

At this point, we are able to estimate the precision of a polarization prediction given the findings of previous sections. Here, we focus on presenting and discussing the results for the binary system CD−30° 11223. Derivations for all the expressions that will be used are given in Appendix A. The 'plus' and 'cross' polarizations of GW emitted by CD−30° 11223 change the length of the photon path by $\Delta L_+(t)$ and $\Delta L_\times(t)$ respectively. The numerical values of their amplitudes depend on the position of LISA relative to the binary system (which is described through the angles ϕ and ψ illustrated in Fig. 2b) and are given by:

$$\frac{\Delta L_+}{L} \approx 4.2 \times 10^{-22} \cos(2\phi) \tag{18a}$$

$$\sigma_+ \approx 2\sqrt{0.02^2 + \Delta_\phi^2 \tan(2\phi)^2} \tag{18b}$$

$$\frac{\Delta L_\times}{L} \approx -1.0 \times 10^{-22} \sin(2\phi) \tag{18c}$$

$$\sigma_\times \approx 2\sqrt{0.03^2 + \Delta_\phi^2 \cot(2\phi)^2} \tag{18d}$$

$$\frac{\Delta L_+}{\Delta L_\times} \approx -4.1 \times \frac{\cos(2\phi)}{\sin(2\phi)} \tag{18e}$$

The polarization amplitudes depend on the unresolved orbital orientation angle ϕ periodically. The relative uncertainties σ_+ and $\sigma_\times$ can be multiplied by the amplitudes to give the absolute error of the polarization prediction. They depend partly on observational errors listed in Table 1 and partly on the error in the orientation angle ϕ. In Fig. 1, we have shown the full range of possible polarization amplitudes and uncertainties given by different errors in the orientation angle. A convenient way to express the total accuracy of a polarization prediction is the square sum of the relative uncertainties:

$$\mathcal{R}^2 = \sigma_+^2 + \sigma_\times^2 \approx 0.08^2 + \frac{40}{3}\Delta_\phi^2 \tag{19}$$

Here, Δ_ϕ is the error in the measurement of the angle ϕ, while the fixed numerical value of 0.08^2 is the combined uncertainty arising from the measurements given in Table 1. Briefly, $\mathcal{R}$ is a measure of the total error that can be expected from all the uncertainties in the observational data about the binary system (Table 1), along with the error in the angle ϕ arising from the intensity interferometry approach. As seen in previous paragraphs, Δ_ϕ can be reduced with longer observation times or with more ambitious telescope array combinations. The errors arising from the parameters in Table 1 might also decrease as more precise measurements are published in the near future. In Fig. 7, we show the uncertainty of the polarization prediction for the binary system CD–30° 11223 with the available measurements as a function of observation time for intensity interferometry. Interestingly, just a few dozen nights of observation with the VLT + ACHSO or a single day with the VLT+ELT combination essentially reduce the error in the orientation angle ϕ to zero.

5 DISCUSSION AND CONCLUSION

This paper presents a method to resolve the orientation of a LISA verification binary and thereby produce a prediction for its GW amplitudes. The idea is to resolve the elongation of the tidally

stretched star via intensity interferometry, in order to deduce the rotation axis of the binary system, which in turn determines the polarization amplitudes of the GW. We look at a promising binary system: CD–30° 11223, comprised of a hot sdB and a WD.[2] We deduce the elongation of the stretched sdB via two methods: using Roche potential and using radiant flux variations. Assuming an incoherent source we compute numerically the intensity interference measurable on the Earth's surface. As the Earth revolves around itself, the baselines move over the interferometric (u, v) plane inhomogeneously. We compute the effective time spent collecting data (counting coincidence photons) at each point of the (u, v) plane. This yields an effective S/N, which we use to recover the orientation of the ellipticity. For a mock signal induced by an angle $\phi = 0$, we compute the posterior distribution of the binary inclination angle given the mock signal and noise. Our estimates for the binary system CD−30° 11223, as shown in Figs 7 and 1, suggest that the intensity interferometry approach using ACHSO can measure the orientation angle ϕ to a few degrees ($\sim$5°) in a large but not unimaginable amount of observation hours ($\sim$ 600 h). However, using the combination of ACHSO and VLT would achieve the same accuracy in less than a tenth of the time. For the case of VLT and ELT, only a single night of observation would be required to constrain the uncertainty to roughly 1° at 2σ confidence level.

There are several considerations that might increase the prospects of this methodology in the years leading to the launch of LISA. As an example, the S/N ratio increases linearly with the quantum efficiency of the photon detectors and also increases as the inverse square root of their resolution time. Both of these technologies are likely to improve, thus reducing the time needed to achieve the desired precision. Measurements of the orbital parameters of verification binaries are also likely to improve significantly in coming years, further reducing the uncertainties in the polarization prediction. These points argue that intensity interferometry will be an essential piece of the 'multimessenger puzzle' needed to predict and measure GW.

There are however, a number of caveats that were not included in our estimates.

On the experimental side, we are assuming the viability of some technologies that are currently under development. The most difficult challenge at telescopes would be the deployment of kilopixel photon counters. This requires dispersing light so that each pixel gets a different narrow wavelength band. Precise wavelength calibration is not required, just reproducibility in the sense that corresponding pixels in different detectors get the same wavelength band. The basic idea has been discussed in the context of intensity interferometry (see fig. 3 in Horch et al. 2016). Even though the implementation of such technology on current telescope arrays seems ambitious, it does not have to be implemented now, but rather in a dozen or so years. In our estimation, this is a reasonable proposal since prototypes already exist. In a sense, LISA itself is the most ambitious piece of technology that we are assuming in this work.

On the side of our analysis, the method of fitting noisy mock data presented in Section 2.3.3 assumes that the shape of the source is fixed and homogeneous. In reality, the light profile of the source will decay towards the edges because of limb darkening. Moreover, the projection of the tidally stretched star on the sky is not always teardrop shaped for an edge-on binary such as CD−30° 11223. Rather, it will vary from circular to teardrop depending on the phase of the orbit. Because of the technicalities of intensity interferometry,
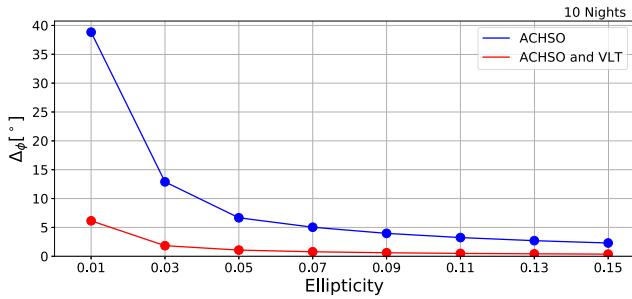
---

[2]The sdB being actually gigantic compared to the WD.

Figure 8. We plot the remaining uncertainty Δ_ϕ in the orientation angle ϕ after 10 nights of observation for a spheroidal source with the same parameters as CD−30° 11223, but with varying ellipticities. The blue points are produced using ACHSO and the red using ACHSO and VLT. As expected, strongly elliptical sources can be resolved more quickly.

it is not straightforward to estimate how the shape and light profile of the source affects S/N. To get an idea for the relevance of the source's shape, we ran several realizations of a homogeneous source with different ellipticities. We show how it affects the uncertainty on the orientation angle for 10 nights of observation in Fig. 8. The 2D projection of a tidally stretched star on the sky will have an apparent ellipticity that changes direction and varies periodically. On the one hand, we might expect these factors to cut the signal by a factor of 2–4. On the other hand, if one were to implement a light profile and the variation of the source's shape in the fitting process, they might actually lead to more efficient recover of the orientation.

Another problem in the parameter fitting is the fact that we do not explicitly model many possible sources of noise that might affect the coincidence rate of photons. An example would be atmospheric effects, which might affect the signal in a manner roughly proportional to the attenuation of blue light in the atmosphere.

Lastly, we have chosen to analyse the binary system CD−30° 11223 precisely because it was a promising candidate for this methodology. There are numerous intrinsic source properties, for example, radiant intensity, effective temperature, amount of tidal stretching, angular size, orientation, and location on the sky, that affect the efficacy of intensity interferometry. It is not straightforward to extrapolate the effects of these parameters from one single example, with the possible exception of the radiant intensity of the source which explicitly appears in the S/N expression. For example, a system with Roche lobe overflow would present a more non-circular target to resolve with intensity interferometry. There are such systems among the LISA verification binaries, but they are even fainter and smaller in angular size than CD−30° 11223.

Are there other possibilities for detecting the orientation angle of this system? One possibility is to investigate occultations of the binary system by asteroid belt objects (Benbow et al. 2019). However, while asteroid occultations of stars are common events, occultation of a given star would be exceedingly serendipitous, and moreover it is not clear what the observational signature of an elliptical source by an irregular source would be (cf. Richichi & Glindemann 2012). Another option could be detecting the polarized light of the sdB, reflected by the WD (Schmid 1992; Schmid & Schild 1997). However, the WD itself is not resolvable with current technology, let alone the reflected light due to the sdB. Thus, we believe intensity interferometry is the most optimistic method.

In short, there is still plenty of work to be done to direct, refine, and constrain the possibilities of the intensity interferometry approach. The combination of ACHSO (which has considerably different optical properties and a much improved PSF than CTA)

and VLT is probably potent enough to resolve the orientation angle of confirmation binaries other than CD−30° 11223. Even though it is ambitious, the combination can be made even more powerful using the ELT. The telescope arrays could be set up for intensity interferometry during moonlit nights and would therefore not compete with other high-priority observations. By exploiting a few days per month, it is within the realms of possibility to start constraining the polarization predictions of many LISA confirmation binaries.

DATA AVAILABILITY STATEMENT

No new data were generated or analysed in support of this research.

REFERENCES

Abbott B. P. et al., 2017, Phys. Rev. Lett., 119, 141101
Abeysekara A. U. et al., 2020, Nat. Astron., preprint (arXiv:2007.10295)
Acciari V. A. et al., 2020, MNRAS, 491, 1540
Acharya B. S. et al., 2013, Astropart. Phys., 43, 3
Ajith P. et al., 2008, Phys. Rev. D, 77, 104017
Avni Y., Schiller N., 1982, ApJ, 257, 703
Babak S. et al., 2017, Phys. Rev. D, 95, 103012
Benbow W. et al., 2019, Nat. Astron., 3, 511
Berti E., Cardoso V., 2006, Int. J. Mod. Phys. D, 15, 2209
Berti E., Cardoso J., Cardoso V., Cavaglià M., 2007, Phys. Rev. D, 76, 104044
Blanchet L., 2019, Int. J. Mod. Phys. D, 28, 1930011
Buonanno A., Pan Y., Baker J. G., Centrella J., Kelly B. J., McWilliams S. T., van Meter J. R., 2007, Phys. Rev. D, 76, 104049
Dravins D., LeBohec S., Jensen H., Nuñez P. D., 2013, Astropart. Phys., 43, 331
Einstein A., 1916, Ann. Phys., 354, 769
Filloux C., de Preitas Pacheco J. A., Durier F., de Araujo J. C. N., 2012, J. Phys. Conf. Ser, 363, 012046
Foellmi C., 2009, A&A, 507, 1719
Gaug M., Fegan S., Mitchell A. M. W., Maccarone M. C., Mineo T., Okumura A., 2019, ApJS, 243, 11
Geier S. et al., 2013, A&A, 554, A54
Guerin W., Rivet J.-P., Fouché M., Labeyrie G., Vernet D., Vakili F., Kaiser R., 2018, MNRAS, 480, 245
Hanbury Brown R., 1974, The Intensity Interferometer: Its Application to Astronomy. Taylor and Francis, Oxfordshire, England
Hanbury Brown R., Twiss R. Q., 1956, Nature, 178, 1046
Hanbury Brown R., Twiss R. Q., 1957, Proc. R. Soc. Lond. Ser. A, 242, 300
Hanbury Brown R., Davis J., Allen L. R., 1974, MNRAS, 167, 121
Heller M. et al., 2017, Eur. Phys. J. C, 77, 47
Horch E. P. et al., 2016, in SCSI: the Southern Connecticut Stellar Interferometer, Proc. SPIE, Vol. 9907. p. 99071W
Huerta E. A. et al., 2017, Phys. Rev. D, 95, 024038
Hu X.-C. et al., 2018, Class. Quantum Gravity, 35, 095008
Isi M., Pitkin M., Weinstein A. J., 2017, Phys. Rev. D, 96, 042001
Jedrzejewski R. I., Hartig G., Jakobsen P., Crocker J. H., Ford H. C., 1994, ApJ, 435, L7
NoKieda D. B., LeBohec S., Cardon R., 2019, in Proc. 36th ICRC, preprint (arXiv:1908.03095)
Kupfer T. et al., 2018, MNRAS, 480, 302
Le Bohec S., Holder J., 2006, ApJ, 649, 399
Lester K. V., Gies D. R., Schaefer G. H., Farrington C. D., Monnier J. D., ten Brummelaar T., Sturmann J., Vargas N., 2019, AJ, 157, 140

Mandel L., Wolf E., 1995, Optical Coherence and Quantum Optics, Cambridge University Press, Cambridge

Matthews N., LeBohec S., 2019, in Proc. 36th ICRC, preprint (arXiv:1908.03587)

Matthews N., Kieda D., LeBohec S., 2018, J. Mod. Opt., 65, 1336

Peters P. C., Mathews J., 1963, Phys. Rev., 131, 435

Philippoz L., Boîtier A., Jetzer P., 2018, Phys. Rev. D, 98, 044025

Richichi A., Glindemann A., 2012, A&A, 538, A56

Robson T., Cornish N. J., Liu C., 2019, Class. Quantum Gravity, 36, 105011

Rou J., Nuñez P. D., Kieda D., LeBohec S., 2013, MNRAS, 430, 3187

Sakurai S., Depaoli D., López-Coto R., 2019, in Proc. 36th ICRC, preprint (arXiv:1907.09357)

Schaefer G., 2003, in Fernández-Jambrina L., González-Romero L.-M., eds, Binary Black Holes and Gravitational Wave Production: Post-Newtonian Analytic Treatment, p. 195

Schmid H. M., 1992, A&A, 254, 224

Schmid H. M., Schild H., 1997, A&A, 321, 791

Stroeer A., Vecchio A., 2006, Class. Quantum Gravity, 23, S809

Tayabaly K., Spiga D., Canestrari R., Bonnoli G., Lavagna M., Pareschi G., 2015, in Society of Photo-Optical Instrumentation Engineers (SPIE) Conference Series. p. 960307

Weiss S. A., Rupert J. D., Horch E. P., 2018, in Optical and Infrared Interferometry and Imaging VI, p. 107010X

Wollman E. E., Verma V. B., Lita A. E., Farr W. H., Shaw M. D., Mirin R. P., Woo Nam S., 2019, Opt. Exp., 27, 35279

Zahn J. P., 1989, A&A, 220, 112

Zampieri L. et al., 2016, in Intensity interferometry with Aqueye+ and Iqueye in Asiago, Proc. SPIE, Vol. 9907, p. 99070N

APPENDIX A: COMPUTATION OF THE WAVEFORM AND ERROR ESTIMATION

In this section, we briefly summarize how one goes from the generation of GWs in an astrophysical system to their detection back here around Earth. For the sake of clarity, and in view of the application presented in Section 2, we adopt some simplifying assumptions.

First, we assume that the system generating the GWs is an isolated binary of compact objects. This allows us to only consider the pure signal originating from the two bodies. Secondly, we assume that the angular momentum vector of the binary's orbit does not change significantly over the period of the measurement, thus neglecting the complicated effects of spin–spin and spin–orbit coupling on orbital motion. This allows us to find a unique and convenient coordinate system in which to describe the process. We also simplify the experimental side by considering only one detector 'arm'. In other words, we imagine LISA as consisting of only two satellites exchanging photons. This allows us to not have to keep track of the relative orientation of every pair of satellites with respect to the source of GWs. Finally, we assume perfect knowledge about the binary system's physical parameters, as well as its orientation in space with respect to our idealized LISA arm. This will allow us to calculate an unique prediction for both polarization amplitudes.

We find a convenient coordinate system among the many possible choices, as detailed in Section 2. In this paper, we align the z-axis with the 'line of sight direction' from the binary's centre of mass to the mid-point of our idealized LISA arm. This choice fixes the 'x–y' or 'transverse' plane in which GWs will produce a measurable strain. We then align the y-axis with the projection of the orbit's angular momentum in the transverse plane. The chosen coordinate system is illustrated in Fig. 2(a). This choice will greatly simplify the the explicit construction of the mass quadrupole moment of the binary system CD−30° 11223.

Returning to the general case, this choice of coordinates fixes a unique mass quadrupole moment for the system. It is given by a 3×3 symmetric matrix $\mathbf{M}$ that can be used as input for the quadrupole formalism (Einstein 1916; Schaefer 2003) to obtain the spatial part of the linear metric perturbation tensor $\boldsymbol{h}$:

$$\boldsymbol{h}(t) = \frac{2G}{c^4 d} \ddot{\mathbf{M}}(t_d) \tag{A1}$$

Here, G is the gravitational constant, c is the speed of light, d is the distance between the detector and the source, and $t_d = t - d/c$ is the retarded time. The 'plus' and 'cross' polarizations h_+ and $h_\times$ are commonly used measures of the strain produced by the metric perturbation along the transverse plane. In these coordinates, they are found by projecting the tensor $\boldsymbol{h}$ in the line of sight direction and removing its trace:

$$h_+(t) = \frac{G}{c^4 d} \left(\ddot{M}_{11}(t_d) - \ddot{M}_{22}(t_d) \right)$$
$$h_\times(t) = \frac{2G}{c^4 d} \left(\ddot{M}_{12}(t_d) \right) \tag{A2}$$

We now relate the physical amplitudes to those measured by an experimental setup. In our coordinates, an idealized LISA arm consists of a thin line of length L centred somewhere along the z-axis. The two independent polarization amplitudes are modified by two additional factors. The first is the angle ϕ between the y-axis and the projection of the detector arm on the transverse plane. The second is the angle ψ that describes the intersection of the arm with the transverse plane. These two angles are illustrated in Fig. 2(b). The former affects the relative strength of the measured polarization amplitudes while the latter simply reduces both amplitudes if the arm is tilted with respect to the transverse plane. We apply these projections as follows:

$$h_+(t) \to \cos(2\phi) \cos(\psi) h_+(t)$$
$$h_\times(t) \to \sin(2\phi) \cos(\psi) h_\times(t) \tag{A3}$$

Lastly, we consider the fact that the measurement of the strain is not instantaneous. If the detector has a length L, a photon travelling along the arm will take a time L/c to complete its path. To represent this fact, one integrates the strain along a photon's path:

$$h_+(t) \to \frac{c}{L} \int_{t-L/c}^{t} h_+(t') \mathrm{d}t' \equiv \frac{\Delta L_+(t)}{L}$$
$$h_\times(t) \to \frac{c}{L} \int_{t-L/c}^{t} h_\times(t') \mathrm{d}t' \equiv \frac{\Delta L_\times(t)}{L} \tag{A4}$$

Note that the length of the photon path is affected by the strain as $\mathrm{d}L = (1 + h)c\mathrm{d}t$, so $L_{\text{strained}} = L + \Delta L$. Now we can specialize the formulae to the case of the binary system CD−30° 11223. The largest contribution to the mass quadrupole moment comes from the orbital motion of the two bodies around their centre of mass. Since CD−30° 11223 is an isolated binary with a very short period we can assume that is on a very low eccentricity orbit (Zahn 1989). We describe the orbit through the separation vector $\boldsymbol{r}(t)$ between the stars:

$$\boldsymbol{r}(t) = \begin{pmatrix} r_x(t) \\ r_y(t) \\ r_z(t) \end{pmatrix} = R \begin{pmatrix} \cos(\omega t) \\ \sin(\omega t) \cos(\mathcal{I}) \\ -\sin(\omega t) \sin(\mathcal{I}) \end{pmatrix} \tag{A5}$$

Here, R is the radial separation and ω is the orbital frequency. We can arbitrarily set the true anomaly (phase) to zero to simplify the calculations. The mass quadrupole moment $\mathbf{M}$ for two point masses is then given by (see e.g. Peters & Mathews 1963):

$$M_{ij}(t) = \mu r_i(t) r_j(t) \tag{A6}$$

where μ is the reduced mass of the binary. Its magnitude is given by the reduced mass multiplied by the square radial separation (μR^2). The second largest contribution to the mass quadrupole moment comes from the tidal stretching of the sdB. It turns out, that this and all other smaller contributions are negligible. Indeed, for a spheroid with principal semi-axes (b, a, a) and a mass m_{sdB} the magnitude of the quadrupole M_{sph} is given by:

$$M_{sph} = \frac{2}{5} m_{sdB}(b^2 - a^2) \tag{A7}$$

It can be restated in terms of the parameter $\kappa = a/b$ used in Section 3 and the mean geometric radius $r_{gm} = \sqrt[3]{a^2 b}$ of the spheroid:

$$M_{sph} = \frac{2}{5} m_{sdB} r_{gm}^2 \left(\frac{1 - \kappa^2}{\kappa^{4/3}} \right) \tag{A8}$$

The ratio between the sdB's quadrupole M_{sph} and the orbit's quadrupole M is very small for our system's parameters:

$$\frac{M_{sph}}{M} = \frac{2 m_{sdB}}{5\mu} \frac{r_{gm^2}}{R^2} \left(\frac{1 - \kappa^2}{\kappa^{4/3}} \right) \approx 0.6 \text{ per cent} \tag{A9}$$

The direction of tidal stretching is always radial and therefore its variation shares the orbital frequency. For this reason, if the tidally induced quadrupole is only 0.6 per cent of the orbit induced quadrupole the amplitude of the GW produced by it will only be 0.6 per cent of the total amplitude. It is safe to neglect it along with all other smaller contributions.

Now we can proceed with the polarization prediction. Using the formulae above we find:

$$\frac{\Delta L_+(t)}{L} = \frac{\Delta L_+}{L} \cos \left(-\frac{L\omega}{c} + 2\omega t_d \right)$$
$$\frac{\Delta L_\times(t)}{L} = \frac{\Delta L_\times}{L} \sin \left(-\frac{L\omega}{c} + 2\omega t_d \right) \tag{A10}$$

where t_d is the retarded time and the amplitudes are given by:

$$\frac{\Delta L_+}{L} = \frac{G\mu R^2 \omega \cos(2\phi) \cos(\psi)(3 + \cos(2\mathcal{I})) \sin \left(\frac{L\omega}{c} \right)}{c^3 d L}$$
$$\frac{\Delta L_\times}{L} = -\frac{4G\mu R^2 \omega \sin(2\phi) \cos(\psi) \cos(\mathcal{I}) \sin \left(\frac{L\omega}{c} \right)}{c^3 d L} \tag{A11}$$

The ratio Q between the two amplitudes is given by:

$$Q = \frac{\Delta L_+}{\Delta L_\times} = -\frac{3 + \cos(2\mathcal{I})}{4 \cos(\mathcal{I})} \frac{\cos(2\phi)}{\sin(2\phi)} \tag{A12}$$

Plugging in the values in Table 1, we find:

$$\omega = \sqrt{\frac{G(m_{sdB} + m_{WD})}{R^3}} \approx 1.49 \text{ mHz} \tag{A13}$$

and:

$$\frac{\Delta L_+}{L} \approx 4.2 \times 10^{-22} \times \cos(2\phi) \cos(\psi)$$
$$\frac{\Delta L_\times}{L} \approx -1.0 \times 10^{-22} \times \sin(2\phi) \cos(\psi)$$
$$Q \approx -4.1 \times \frac{\cos(2\phi)}{\sin(2\phi)} \tag{A14}$$

where the arm length of LISA is $L = 2.5 \times 10^9$ m . These values can be used to produce the polarization predictions once the remaining angles are known. Now we proceed to estimate the error and the
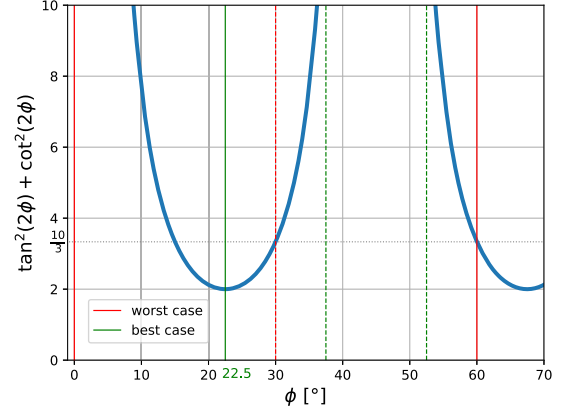

Figure A1. The coefficient $f(\phi)$ in the squared uncertainty $\mathcal{R}^2$ (see equation A16) is periodic within $45°$ ($\pi/4$). The three arms of LISA can sample values of the source's orientation ϕ separated by 60 ($\pi/3$). The worst case (indicated by the red vertical lines) in terms of relative error occurs when one arm samples an angle ϕ lying on a pole of the function $f(\phi)$. In this case, the measurement with other two arms will correspond to a value $f(\phi) = 10/3$. In the best case (indicated by the green vertical lines), one arm samples an angle lying at the minimum of the function $f(\phi)$, such that $f(\phi) = 2$. The periodicity of $f(\phi)$ allows to illustrate by what angles the arms would sample in the best ($22.5°$, $82.5°$, and $142.5°$) and worst case ($0.0°$, $60.0°$, and $120.0°$) in less than $180°$. Here, we show this by means of the dashed coloured lines.

relative uncertainty in the polarization amplitudes. We call the uncertainties σ_+ and $\sigma_\times$. By using Gaussian error propagation, we find:

$$\sigma_+ \approx 2\sqrt{0.02^2 + \Delta_\phi^2 \tan(2\phi)^2}$$
$$\sigma_\times \approx 2\sqrt{0.03^2 + \Delta_\phi^2 \cot(2\phi)^2} \tag{A15}$$

Here, we are considering errors arising from the uncertainties in the parameters m_{sdB}, m_{WD}, ϕ, $\mathcal{I}$, R and d, along with the neglection of the quadrupole moment of the sdB. The square sum of the errors $\mathcal{R}^2$ is given by:

$$\mathcal{R}^2 = \sigma_+^2 + \sigma_\times^2 \approx 0.08^2 + 4\Delta_\phi^2 \left(\tan(2\phi)^2 + \cot(2\phi)^2 \right) \tag{A16}$$

The coefficient $f(\phi) = \tan(2\phi)^2 + \cot(2\phi)^2$ plotted in Fig. A1 is a periodic function with divergent poles at $\phi = n\pi/4$ and minima at $\phi = \pi/8 + n\pi/4$. Since LISA has three arms approximately resembling an equilateral triangle, it can sample three different values of ϕ, evenly spaced by $\pi/3$. The worst possible case in terms of measurement uncertainties occurs if one of these sampled angles lies on a pole of the function $f(\phi)$. In that case, the other two angles will read $n\pi/4 + \pi/3$ and $n\pi/4 + 2\pi/3$. The function $f(\phi)$ evaluated at the latter angles yields a value 10/3. This value represents a 'best of the worst case' scenario and will be used as a reference in the main text. In reality, the space antennas arms will sample many different orientations as they orbit around the Sun. The final formula then reads:

$$\mathcal{R}^2 \approx 0.08^2 + \frac{40}{3} \Delta_\phi^2 \tag{A17}$$